Materials Advances

PAPER

Check for updates

Highly efficient non-noble metallic NiCu nanoalloy catalysts for hydrogenation of nitroarenes†

Yao Sheng, [ID] Xinrui Lin, Shengnan Yue, [ID] Yang Liu, Xiujing Zou, Xueguang Wang [ID] * and Xionggang Lu*

Highly dispersed NiCu alloy nanoparticles supported on carbon-doped silica ($NiCu/C@SiO_2$) were first prepared through one-step impregnation with a mixed solution of nickel nitrate, cupric nitrate and glucose, followed by *in situ* carbothermal reduction. The addition of Cu to the $NiCu/C@SiO_2$ materials not only improved the dispersion of metallic Ni particles, but also significantly enhanced the anti-oxidation ability of the catalyst. The effects of catalyst calcination temperatures and Cu element on the catalytic properties of the $NiCu/C@SiO_2$ materials were investigated for nitrobenzene hydrogenation as a model reaction. The results indicated that the $NiCu/C@SiO_2$-800 catalyst carbonized at 800 °C exhibited the highest activity for the hydrogenation of nitrobenzene with a turnover frequency (TOF) of as high as 46.5 s^{-1}, and the superior catalytic activity of $NiCu/C@SiO_2$ to $Ni/C@SiO_2$ could be attributed to both the smaller Ni particles and the higher TOFs of metallic Ni due to the electronic interaction between the Ni and Cu atoms. The $NiCu/C@SiO_2$-800 catalyst could be recycled at least 10 times without noticeable loss of catalytic performance in the hydrogenation of nitrobenzene, exhibiting better stability compared with the $Ni/C@SiO_2$-800 catalyst. Moreover, the $NiCu/C@SiO_2$-800 catalyst could smoothly transform various substituted nitro aromatics to the corresponding aromatic amines with high selectivities.

1 Introduction

Aromatic amines are crucial industrial intermediates for the manufacture of fine chemicals, agrochemicals, pharmaceuticals and dyestuffs.[1,2] Generally, aromatic amines are obtained by the catalytic reduction or hydrogenation of the corresponding nitroarenes with the aid of metal catalysts using various reducing agents such as hydrazine hydrate, hydrogen gas, formic acid, ammonia borane, and so on.[3–6] Among them, H_2, a low cost, non-toxic, and cleanest hydrogen donor, is recognized as the most ideal reducing agent for the hydrogenation of nitro aromatic compounds in industrial production. Pt-based catalysts are the most common catalysts employed in hydrogenation of nitroarenes because of their high intrinsic activity for H_2 activation and dissociation, while their scarcity and high cost hinder their widespread application.[7,8]

State Key Laboratory of Advanced Special Steel, School of Materials Science and Engineering, Shanghai University, 99 Shangda Road, BaoShan District, Shanghai 20444, China. E-mail: wxg228@shu.edu.cn

In recent years, non-noble transition-metal based nanoparticles (*e.g.* Fe, Co, Ni, and Cu) have been extensively investigated to develop efficient catalysts for the hydrogenation reaction,[9–11] among which Ni shows great promise to replace the noble metal in hydrogenation of nitroarenes due to the low cost and availability.[12–15] But these supported Ni catalysts still have two major drawbacks in hydrogenation of nitroarenes: (i) although Ni is active in this reaction with strong reducing agents, such as $NaBH_4$ and hydrazine hydrate, it shows no or low catalytic activity when using the cost-effective H_2 as a hydrogen source; (ii) Ni catalysts generally suffer from poor stability, due to the surface oxidation of Ni nanoparticles. The alloying chemistry strategy offers a promising pathway to modify the electronic structure and geometric characteristics of Ni catalysts, leading to Ni-based alloy catalysts with enhanced catalytic performance compared to pure Ni. For example, NiCu alloy, a typical inexpensive catalyst, has exhibited superior activities in various fields such as furfuryl alcohol hydrogenation,[16] hydrogen generation from hydrous hydrazine,[17] and nitrile synthesis from alcohols.[18] However, the NiCu alloy nanoparticles in the previous reports were always larger than 10 nm, which limited their catalytic hydrogenation activity. What's more, systematic studies on NiCu

bimetallic catalysts in hydrogenation of nitroarenes into aromatic amines are still rare. Therefore, the development of NiCu bimetallic catalysts as highly efficient and stable catalysts for hydrogenation of nitroarenes with H_2 as the reducing agent is crucially important.

In this work, we report the fabrication of carbon-doped silica-supported NiCu bimetallic alloy nanoparticles (NiCu/C@SiO$_2$) *via* a simple one-step impregnation method, followed by *in situ* carbothermal reduction at different temperatures. The obtained NiCu/C@SiO$_2$ catalysts exhibited high catalytic activity and excellent stability for hydrogenation of nitroarenes to aromatic amines using H_2 as the reducing agent. The presence of Cu and catalyst calcination temperatures were found to have a significant effect on the catalytic performance of the NiCu/C@SiO$_2$ materials.

2 Experimental

2.1 Materials

Commercial SiO$_2$ was purchased from Huating (Shanghai) Nano Science & Technology Co., Ltd. Before use, the SiO$_2$ powder was washed and calcined at 550 °C for 6 h to remove water and impurities. Ni(NO$_3$)$_2$·6H$_2$O (AR), Cu(NO$_3$)$_2$·3H$_2$O (AR), Fe(NO$_3$)$_3$·9H$_2$O (AR), Co(NO$_3$)$_2$·6H$_2$O (AR), glucose (AR), and all nitro compounds were purchased from Sinopharm Chemical Reagent Co., Ltd. All chemicals and solvents were commercially available and used as received without further treatment. Deionized water was applied for all aqueous solution preparation. All gases (H_2, N_2, and He) used for catalyst preparation and reactions were of ultra-high purity.

2.2 Synthesis of the catalysts

The NiCu/C@SiO$_2$ catalysts were synthesised by a facile one-step impregnation method followed by carbonization at different temperatures under a N_2 atmosphere. In a typical process, 5 g of Ni(NO$_3$)$_2$·6H$_2$O, 1 g of Cu(NO$_3$)$_2$·3H$_2$O, and 2 g of glucose were added into a 250 mL beaker and dissolved in 60 mL of deionized water at room temperature. Afterward, 5 g of commercial SiO$_2$ powder was added into the above solution and the mixture was evaporated under stirring at 60 °C to remove all the water. Subsequently, the obtained solid was calcined at 750–900 °C for 1 h under N_2 flow with a flow rate of 30 mL min^{-1}. The heating rate of carbonization was set as 2 °C min^{-1}. The obtained bimetallic catalysts were denoted as NiCu/C@SiO$_2$-T, where T represents the carbonization temperature. As controls, Ni/C@SiO$_2$-800 and Cu/C@SiO$_2$-800 monometallic catalysts were synthesized in a similar way with only nickel or copper salt used in the synthesis process; C@SiO$_2$-800, NiOCuO@SiO$_2$-800, FeCu/C@SiO$_2$-800, and CoCu/C@SiO$_2$-800 were prepared following an identical one-step route with aqueous solutions containing the same mass percentages of the metal and/or carbon sources; the NiCu@SiO$_2$–H$_2$-800 was obtained by the reduction of the NiOCuO@SiO$_2$-800 at 800 °C for 1 h under a 30 vol% H_2/N_2 flow.

2.3 Catalyst characterization

N_2 adsorption–desorption isotherms of the samples were measured at −196 °C using a Micromeritics surface area and porosity analyzer (ASAP-2020). Prior to measurement, the samples were degassed at 200 °C for 6 h under vacuum. On the basis of the isotherm data, the specific surface areas (S_{BET}) were calculated using the Brunauer–Emmett–Teller (BET) method. The pore volume and pore diameter were obtained by the Barrett–Joyner–Halenda (BJH) method based on the adsorption branch of the isotherm. Inductively coupled plasma atomic emission spectrometry (ICP–AES) with a PerkinElmer emission spectrometer was used to measure the bulk Ni and Cu contents in the as-prepared products. Powder X-ray diffraction (XRD) patterns were obtained on a Rigaku D/MAX-2200 diffractometer with Cu Kα radiation (λ = 0.1542 nm) and a scanning rate of 8° min^{-1} (2θ = 10° to 90°) at room temperature. Transmission electron microscopy (TEM) and high-resolution transmission electron microscopy (HRTEM) images were collected using a JEOL JEM-2010 instrument operated at 200 kV. Scanning TEM high angle annular dark field (STEM-HAADF), elemental mapping, and linear scanning imaging were conducted on a JEOL JEM-2100F with an accelerating voltage of 200 kV. X-ray photoelectron spectroscopy (XPS) measurements were performed on a Thermo Scientific K-Alpha XPS system with scanning monochromatic X-ray Al Kα radiation as the excitation source (16 mA, 12.5 kV, 1486.6 eV), and the base pressure of the analysis chamber was 5.0×10^{-7} mbar. The binding energies of all elements were calibrated using C 1s as the reference energy (C 1s = 284.6 eV). Dynamic CO pulsed chemisorption was performed using an AutoChem1 II 2920 automatic analyzer equipped with a TCD. The sample was loaded into a quartz reactor and pre-reduced under H_2 flow at 400 °C for 2 h at a rate of 10 °C min^{-1}. Then the sample was purged with He at 400 °C for 2 h and cooled to 200 °C under a He flow. The CO pulse was repeatedly injected until the response from the detector showed no further CO uptake after consecutive injections.

2.4 Catalytic reactions and product analyses

The chemoselective hydrogenation of nitro aromatics with H_2 as the reducing agent was conducted in a stainless-steel autoclave (Shanghai Yanzheng Experimental Instrument Co., Ltd, 200 mL) with an external stirring and temperature controller. In a typical experiment, 50 mmol of nitrobenzene, 20 mL of ethanol, and 5 mg of catalysts were added to the reactor. Before starting the reaction, the reaction system was purged with 5 bar of H_2 three times to remove the air and heated to 120 °C from room temperature. When the temperature reached 120 °C, the pressure was increased to 2 MPa within 5 min, and the stirring speed was kept at 800 rpm. After the completion of the reaction, the reactor was cooled down to room temperature and the remaining H_2 was carefully released. The liquid solution was rapidly separated from the reaction mixture by filtration for further analysis. Qualitative analysis of the liquid phase was performed by gas chromatography–mass spectrometry (GC–MS) (Shimadzu GCMS-QP 2010 Plus) and GC (Varian CP-3800)

with *n*-decane as the internal standard. Each reaction was repeated at least three times to ensure a carbon balance of more than 98%. For the reuse of the catalyst, the hydrogenation of nitrobenzene was conducted on a 4 mmol scale (200 mmol of nitrobenzene, 80 mL of ethanol, and 20 mg of catalysts) at 120 °C and 2 MPa. After the reaction, the catalyst was recycled by centrifugation and then washed thoroughly with ethanol. Finally, the recycled catalyst was dried overnight in an oven at 60 °C and then used for the next run without any reactivation or purification. The TOF was calculated from the specific reaction rate and dispersions of Ni species:

$$TOF = NC/(M \times t)$$

where N is the initial number of moles of the substrate; C is the conversion of substrates after reaction time t; M is the loading of Ni $\times$ m (cat.) $\times$ (Ni dispersion)/58.693; t is the reaction time (s).

3 Results and discussion

3.1 Characterization of NiCu/C@SiO$_2$ catalysts

The synthesis of the NiCu/C@SiO$_2$ catalysts was achieved *via* a facile one-step impregnation method followed by carbonization at a high temperature under a N$_2$ atmosphere (Fig. 1a). First, in the impregnation process, the glucose molecule, and Ni^{2+} and Cu^{2+} metal ions were spontaneously adsorbed onto the surface

of the mesoporous SiO$_2$ because of the capillary force. During the carbonization step, glucose was used as the carbon source, which progressively decomposed, condensed, and was transformed to a carbon matrix on the SiO$_2$ surfaces. Simultaneously, the metal ions were reduced to generate metal nanoparticles, assisted by the reducing gases (*e.g.* CO) and residual carbon came from the *in situ* carbothermal reduction process. Finally, through a facile one-step impregnation combined with *in situ* carbothermal reduction, carbon-doped porous silica-supported NiCu bimetallic alloy nanoparticles were generated.

The crystalline phase and structure of the as-prepared mono and bimetallic catalysts were analyzed by XRD (Fig. 1b). For the monometallic Ni/C@SiO$_2$-800 catalyst, three intense and strong diffraction peaks were observed at 44.6°, 51.9°, and 76.6°, which could be assigned to the (111), (200), and (220) crystal planes of face-centered-cubic structured metallic Ni^0 (JCPDS 04-0850), respectively.[19,20] The XRD analysis of the monometallic Cu/C@SiO$_2$ catalyst showed similar sharp characteristic peaks at 43.4°, 50.6°, and 74.2°, corresponding to (111), (200), and (220) of fcc metallic Cu^0 (JCPDS 04-0836), respectively.[21,22] As for the NiCu/C@SiO$_2$-*T* bimetallic catalysts, all of the diffraction peaks lay between those of metallic Cu and Ni, suggesting the formation of an NiCu alloy phase, which was in agreement with the previously reported NiCu bimetallic catalysts.[23,24] It was noteworthy that all NiCu/C@SiO$_2$-*T* bimetallic catalysts showed much weaker XRD peaks compared to those of both
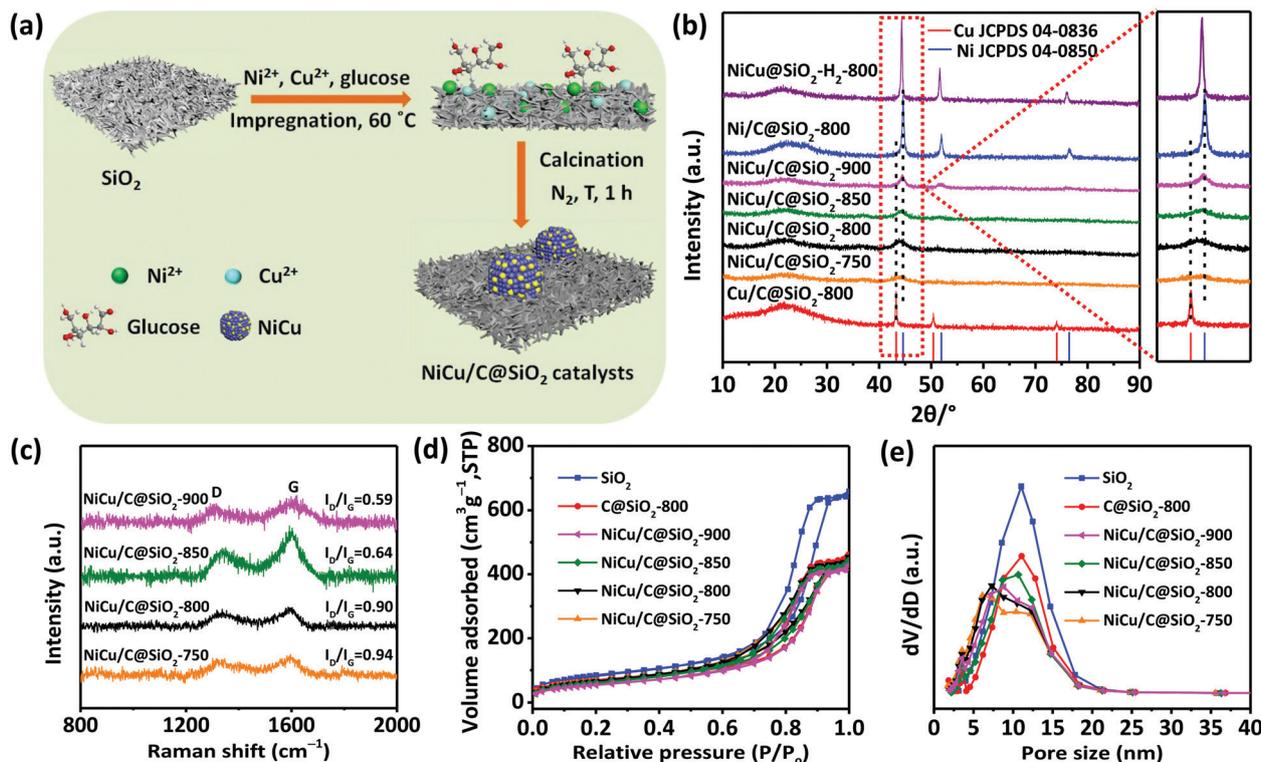

Fig. 1 (a) Schematic representation of the synthesis of NiCu/C@SiO$_2$ catalysts. (b) XRD analysis of the NiCu@SiO$_2$–H$_2$-800, Ni/C@SiO$_2$, Cu/C@SiO$_2$, and NiCu/C@SiO$_2$-*T* catalysts. (c) Raman spectra of the NiCu/C@SiO$_2$-*T* catalysts. (d) N$_2$ sorption isotherms and (e) BJH pore size distributions of the SiO$_2$, C/SiO$_2$-800, and NiCu/C@SiO$_2$-*T* catalysts.

monometallic Ni/C@SiO$_2$-800 and Cu/C@SiO$_2$-800 catalysts, indicating low crystallinity and small particle sizes. Moreover, with increasing carbonization temperatures from 750 to 900 °C, the intensity of the diffraction peaks for NiCu alloys was strengthened, and each individual peak exhibited a gradual shift from pure Cu toward pure Ni as well. The mean crystallite sizes of Ni^0, Cu^0, and NiCu alloy were obtained using the peak width of the (111) crystal plane by the Scherrer equation, and the results are listed in Table S1 (ESI†). The crystallite sizes of NiCu alloys in NiCu/C@SiO$_2$-T samples were enlarged from 4.0 to 6.5 nm when the temperatures were increased from 750 to 900 °C. However, the crystallite sizes of Ni^0 and Cu^0 for Ni/C@SiO$_2$-800 and Cu/C@SiO$_2$-800 samples were 14.0 and 19.9 nm, respectively. For NiCu@SiO$_2$-H$_2$-800, both the intensity of diffraction peaks and the crystallite sizes of the NiCu alloy particles were larger than those of NiCu/C@SiO$_2$-800. These results implied that the alloying of Ni with Cu by *in situ* carbothermal reduction improved the dispersion of NiCu alloy nanoparticles on the catalyst surface, as reported in previous studies.[25,26] Different from the characteristic high intensity peaks of the metallic Ni, Cu, or NiCu alloy phase, a broad reflection peak at $2\theta = \sim 22°$ was observed in all samples, which was attributed to the amorphous silica and/or carbon.[27,28] Although the diffraction pattern of carbon overlapped with silica, the existence of the carbon structures was confirmed by Raman experiments. As shown in Fig. 1c, all the NiCu/C@SiO$_2$-T samples exhibited two characteristic peaks at ~1327 (D band) and ~1599 cm^{-1} (G band), corresponding to the sp^3 carbon atoms and the bond stretching of sp^2 atoms, respectively.[29–31] The intensity ratio (I_D/I_G) of the D and G bands is an index to characterize the graphitization degree of carbon materials. The calculated I_D/I_G values were decreased from 0.94 to 0.59 for the NiCu/C@SiO$_2$-T catalysts when the temperatures were increased from 750 to 900 °C, indicating that the graphitization degrees increased with the calcination temperature.

The actual metal loading and C contents in the final catalysts were measured by ICP and XPS, respectively, and the results are listed in Table S1 (ESI†). The Ni and Cu contents of bimetallic NiCu/C@SiO$_2$-T (T = 750, 800, 850, and 900) catalysts were all located at 13.8 ± 0.1 wt% and 3.6 ± 0.1 wt%, respectively, which were both slightly lower than those of the NiOCuO@SiO$_2$-800, NiCu@SiO$_2$–H$_2$-800, Ni/C@SiO$_2$-800, and Cu/C@SiO$_2$-800, due to the addition of C, Cu and/or Ni. It is noteworthy that the amounts of C incorporated on the NiCu/C@SiO$_2$-T catalyst increased steadily from 8.1% on NiCu/C@SiO$_2$-750, reached a maximum of 10.3% on NiCu/C@SiO$_2$-850 and then decreased to 9.1% on NiCu/C@SiO$_2$-900 catalysts. These results could be explained in terms of the carbonation process of glucose involving the condensation of C organic precursors on the surfaces and the consumption of carbon in the metal reduction. When the temperatures were further increased to 900 °C, the carbonization process was almost finished, while the reduction of metal oxides was ongoing, resulting in the degree of decline in the C contents on the catalyst surfaces.

Brunauer–Emmett–Teller (BET) gas sorption measurements were utilized to investigate the pore structure and surface properties. The N$_2$ adsorption–desorption isotherms and the pore size distribution of SiO$_2$, C@SiO$_2$-800, and NiCu/C@SiO$_2$-T (T = 750, 800, 850, and 900) samples are shown in Fig. 1d and e, respectively. As revealed by Fig. 1d, all samples exhibited characteristic type IV isotherms with clear hysteresis loops, which was an indication of mesoporous materials. Moreover, the pore size distribution revealed that all samples possessed a unique mesoporous structure with an average pore size of around 10–13 nm (Fig. 1e). The mesoporous structure in the catalysts could improve mass transport during the catalytic hydrogenation reaction. However, the specific surface area, pore volume, and pore size of all catalysts had clear decreases compared with those of the pure SiO$_2$ support (Table S1, ESI†) because of the incorporation of Ni, Cu, and C. In the case of the NiCu/C@SiO$_2$-T (T = 750, 800, 850, and 900) samples, the specific surface areas and pore volumes gradually decreased with an increase in the calcination temperature, but the pore size increased with the calcination temperatures, probably because of the blockage of micropores in the support induced by the aggregation or growth of metal particles.

The microstructure and morphology of Ni/C@SiO$_2$, Cu/C@SiO$_2$, and NiCu/C@SiO$_2$-T (T = 750, 800, 850, and 900) catalysts were further characterized by TEM measurements. As shown in Fig. 2a and f, the average particle size of the catalysts was determined to be 13.9 ± 3.6 and 20.0 ± 4.8 nm for the Ni/C@SiO$_2$-800 and Cu/C@SiO$_2$-800, respectively, and some particle agglomeration could be observed. After alloying of Ni and Cu, the particles became clearly smaller. These results could be explained by the fact that the strong interaction between Ni and Cu atoms could prevent particle agglomeration and reduce the particle size of alloys, as reported in a previous study.[32] The particle size of NiCu/C@SiO$_2$-750 was found to be 3.9 nm (Fig. 2b). When the calcination temperatures were increased from 750 to 900 °C, the particle sizes enlarged from 3.9 to 6.4 nm (Fig. 2b–e), which showed a similar tendency to the XRD results. These findings confirmed that the presence of Cu and catalyst calcination temperatures had significant effects on the dispersion and sizes of metal nanoparticles. It is well-established that the metal nanoparticle size is related to the catalytic activity of the catalyst. In addition, it can be seen from Table S1 (ESI†) that the average particle sizes determined from the TEM were approximately equal to the calculated average crystal sizes by XRD, suggesting the single crystalline nature of these metallic nanoparticles. This result was in good agreement with the HRTEM images of the NiCu/C@SiO$_2$-800 catalyst (Fig. 2g), in which the nanoparticles were highly single crystalline, with an interplanar spacing of 0.206 nm located eactly between the characteristic d-spacings of the Ni(111) planes (0.203 nm) and Cu(111) planes (0.209 nm), indicating the formation of face-centred cubic (fcc) NiCu alloys.[33–35] The fine structure of nanoparticles for the NiCu/C@SiO$_2$-800 catalyst was further confirmed by HAADF-STEM analysis. As seen in Fig. 2h, the STEM-based elemental mapping of the NiCu/C@SiO$_2$-800 sample demonstrated the uniform dispersion of the Si, C, Ni, and Cu elements over the support. At the same time, the compositional profile of Cu was completely in
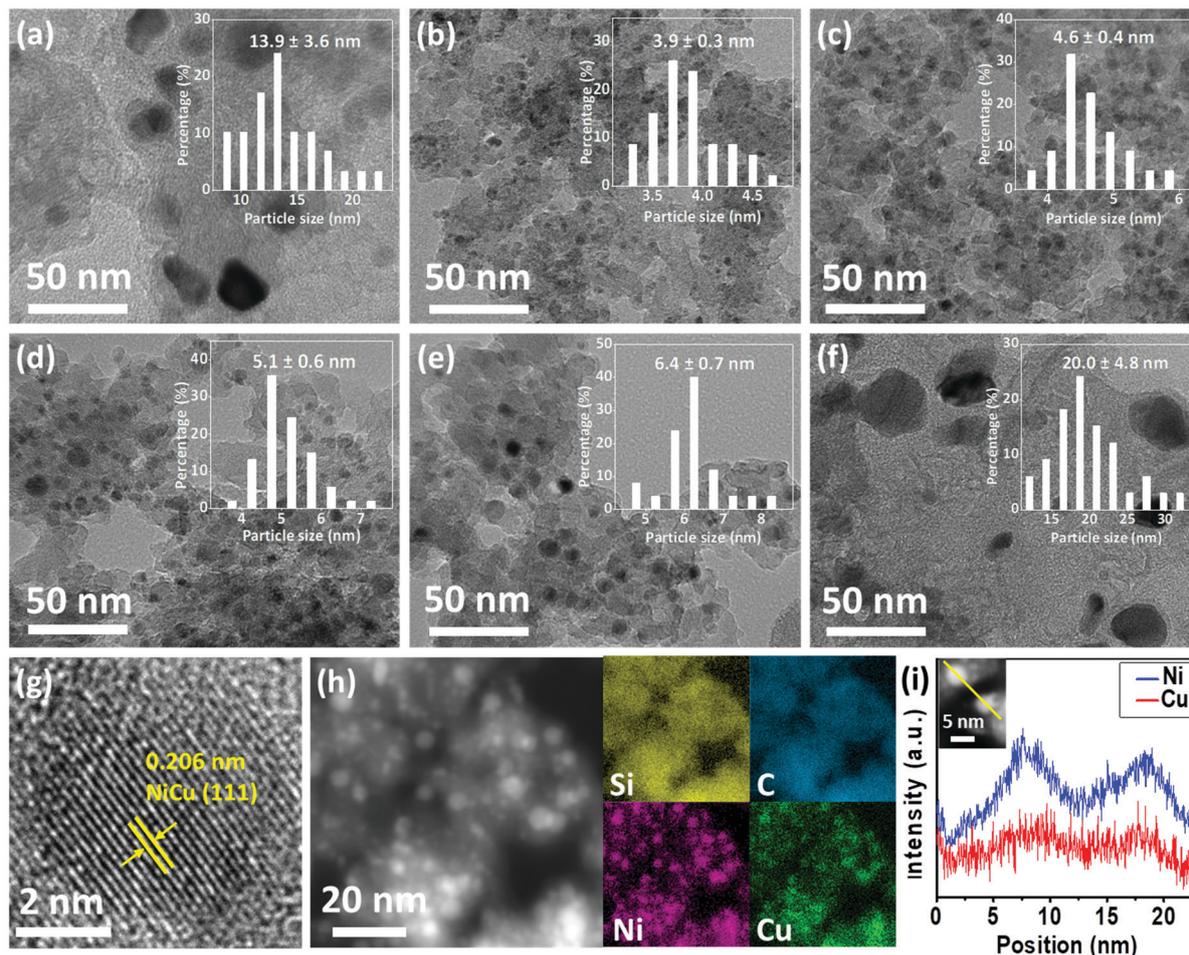
Fig. 2 (a–f) TEM images of the Ni/C@SiO$_2$, NiCu/C@SiO$_2$-750, NiCu/C@SiO$_2$-800, NiCu/C@SiO$_2$-850, NiCu/C@SiO$_2$-900, and Cu/C@SiO$_2$ catalysts. (g–i) HRTEM, HAADF-STEM, elemental mapping, and line scanning images of the NiCu/C@SiO$_2$-800 catalyst, respectively.

agreement with that of Ni in the graph of linear elemental scanning (Fig. 2i), which suggested the existence of a homogeneous NiCu nanoalloy structure.

The elemental chemical states and surface compositions of the mono- and bi-metallic catalysts were obtained from XPS analyses. Fig. 3a shows the Ni 2p$_{3/2}$ XPS spectra of the Ni-containing catalysts. For the monometallic Ni/C@SiO$_2$-800 catalyst, two peaks and one satellite peak were observed at 852.5, 855.5, and 860.9 eV, respectively. The peak at 852.5 eV was attributed to metallic Ni^0 while the peak at 855.5 eV was associated with Ni^{2+},[36,37] and the satellite peak was characteristic of the Ni^{2+} oxidation state. Notably, the Ni 2p$_{3/2}$ peaks for all the bimetallic catalysts shifted gradually to higher binding energies than those for Ni/C@SiO$_2$-800, indicating a change in the near-surface electronic properties of the NiCu alloy nanoparticles.[38–41] In general, the surface electronic properties of active sites are intimately associated with their catalytic activities.[25] The binding energy for the metallic Ni^0 band of the NiCu/C@SiO$_2$-800, NiCu/C@SiO$_2$-850, and NiCu/C@SiO$_2$-900 catalysts was identically shifted by 1.5 eV, and was shifted ∼3 times as much compared to that of the NiCu/C@SiO$_2$-750 catalyst (≈ 0.5 eV). In addition, for all bimetallic NiCu catalysts,

the relative amounts of metallic Ni^0 were increased with the temperatures from 750 to 900 °C, while the Ni^{2+} contents showed a declining trend (Table S2, ESI†). This phenomenon was due to the fact that more Ni oxides were reduced to metallic Ni at a higher temperature in an *in situ* carbothermal reduction process. It is important to point out that the Ni/C@SiO$_2$-800 showed maximum relative peak areas of Ni^{2+} on the catalyst surfaces compared with other bimetallic catalysts (Table S2, ESI†), suggesting that alloying Ni with Cu suppressed the oxidation of Ni. Therefore, the bimetallic catalysts possessed better anti-oxidation ability, even though the small nanoparticles in the bimetallic catalysts were easily oxidized during exposure to air. As seen in Fig. 3b, the Cu 2p$_{3/2}$ peak at 934.1 eV could be assigned to Cu^{2+}, while the main peak around 932.4 eV could be related to Cu$^+$ and/or Cu^0 species.[42,43] To distinguish Cu^0 and Cu$^+$, Auger electron spectroscopy (AES) of the Cu LMM signal (Fig. S1, ESI†) was additionally recorded, indicating the stable coexistence of Cu$^+$ (573.0 eV) and Cu^0 (569.6 eV) on the surface of these catalysts.[44] In addition, as compared to the Cu/C@SiO$_2$-800 catalyst, the main Cu 2p$_{3/2}$ core peaks of the NiCu/C@SiO$_2$-*T* catalysts shifted to lower binding energy values. These results indicated that the Ni species were in an
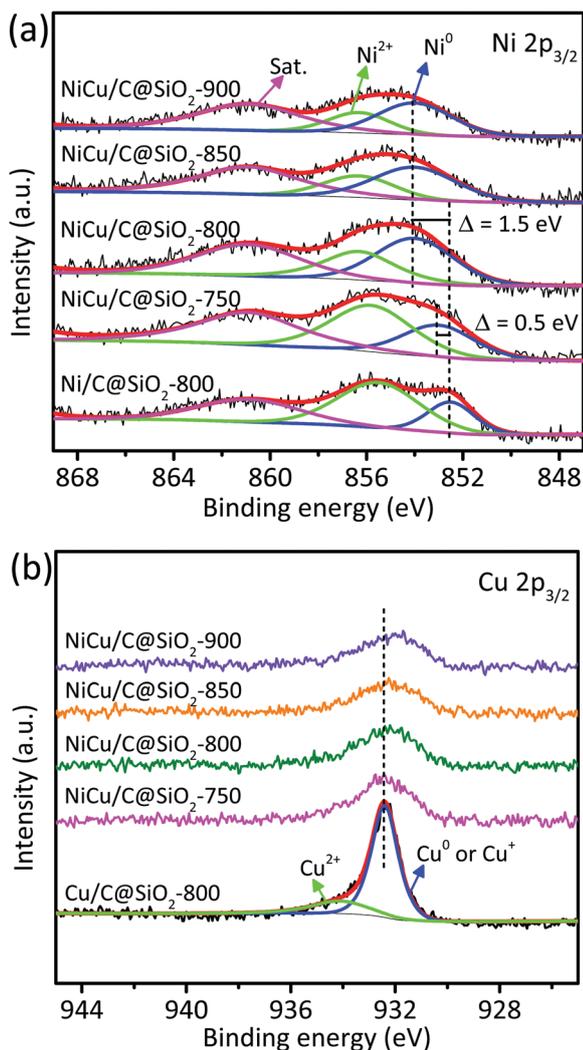
Fig. 3 XPS spectra of the Ni/C@SiO$_2$, Cu/C@SiO$_2$ and NiCu/C@SiO$_2$-T catalysts. (a) Ni 2p and (b) Cu 2p.

Table 1 Catalytic hydrogenation of nitrobenzene to aniline over various catalysts[a]

Entry	Catalyst	Conversion (%)	TOF[b] (s^{-1})	Selectivity[c] (%)
1	C@SiO$_2$-800	0	0	0
2	NiOCuO@SiO$_2$-800	<0.1	0	0
3	Cu/C@SiO$_2$-800	<0.1	0	0
4	NiCu@SiO$_2$–H$_2$-800	12.7	5.6	100
5	Ni/C@SiO$_2$-800	30.1	17.1	100
6	NiCu/C@SiO$_2$-750	75.8	33.5	100
7	NiCu/C@SiO$_2$-800	91.1	46.5	100
8	NiCu/C@SiO$_2$-850	76.9	36.8	100
9	NiCu/C@SiO$_2$-900	63.0	33.1	100
10	FeCu/C@SiO$_2$-800	3.9	1.5	100
11	CoCu/C@SiO$_2$-800	8.7	2.9	100

[a] Reaction conditions: 50 mmol nitrobenzene, 5 mg catalyst, 20 mL ethanol, 2 MPa H$_2$, 120 °C, 0.5 h. [b] Based on dispersions of Ni species in Table S1 (ESI) and initial nitrobenzene conversions of less than 20%. [c] Selectivity at 100% conversion of nitrobenzene.

electron-deficient environment induced by the electron transfer from Ni to Cu by the interfacial electronic interaction.

3.2 Catalytic reactions

Nitrobenzene was first applied as a model compound to study the catalytic performance of the NiCu/C@SiO$_2$ catalysts for the hydrogenation of nitro aromatics to the corresponding anilines under reaction conditions of 120 °C and 2 MPa H$_2$, and the reaction results are summarized in Table 1. As can be seen, the C@SiO$_2$-800, NiOCuO@SiO$_2$-800, and Cu/C@SiO$_2$ displayed almost no catalytic activity in this reaction (entries 1–3), while the NiCu@SiO$_2$–H$_2$-800 and Ni/C@SiO$_2$ showed poor activity with 12.7% and 30.1% nitrobenzene conversions (entries 4 and 5). These results demonstrated that NiO, CuO, and metallic Cu were not effective for the hydrogenation of nitrobenzene, and metallic Ni atoms on the surfaces were active to a certain extent. After alloying of metallic Ni and Cu, the nitrobenzene conversions were dramatically enhanced (entries 6–9). What's more, the carbonation temperature had a substantial effect on the catalytic activities of the NiCu/C@SiO$_2$-T catalysts. The nitrobenzene conversions first increased and then decreased with the increasing carbonation temperature, and showed a maximum value of 91.1% with the NiCu/C@SiO$_2$-800 catalyst. As a result, the TOFs of the NiCu/C@SiO$_2$-800 catalyst exhibited the highest values of 46.5 s^{-1} (Table 1), which, to the best of our knowledge, surpassed those of all the non-noble metal catalysts reported for the hydrogenation of nitrobenzene in previous studies with various reducing agents under similar reaction conditions (Table S3, ESI†). All the NiCu/C@SiO$_2$-T catalysts exhibited much higher catalytic activities than the NiCu@SiO$_2$–H$_2$-800 catalyst, indicating that the presence of carbon from the glucose precursor could greatly improve the performance of the NiCu/C@SiO$_2$-T catalysts for the hydrogenation of nitro aromatics with H$_2$. Furthermore, other Cu-based bimetallic catalysts MCu/C@SiO$_2$-800 (M = Fe and Co) with identical metal loading presented poor catalytic performance for the hydrogenation of nitrobenzene (entries 10 and 11), indicating the indispensable roles of Ni and Cu species in the hydrogenation of the nitro group. In Table 1, all the catalysts exhibited an aniline selectivity of 100% for the hydrogenation of nitrobenzene when the nitrobenzene was completely converted.

To gain more insight into the catalytic activities for nitrobenzene hydrogenation over the mono- and bimetallic catalysts, the product distribution at different reaction time points was recorded (Fig. 4). Considering that the reaction intermediates, such as N-hydroxyaniline, were not stable at high reaction temperatures, the hydrogenation of nitrobenzene was conducted at 50 °C. As shown in Fig. 4, N-hydroxyaniline as the sole intermediate was observed in the hydrogenation of nitrobenzene over both NiCu/C@SiO$_2$-800 and Ni/C@SiO$_2$-800 catalysts, indicating that the aniline synthesis from nitrobenzene hydrogenation over the prepared catalysts mainly followed the direct way.[45–47] The direct way includes the formation of nitrosobenzene, N-hydroxyaniline and finally aniline, following three consecutive hydrogenation steps. In our reaction, no nitrosobenzene intermediates were observed; thus, this indicated that the nitro group was first reduced to the nitroso
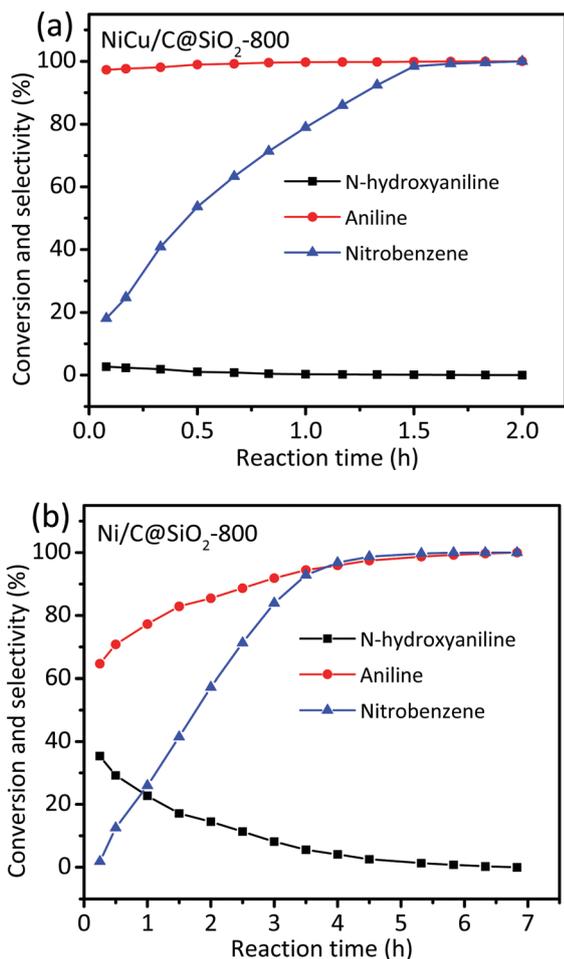
Fig. 4   (a) Time-dependent catalysis by the NiCu/C@SiO$_2$-800. (b) Time-dependent catalysis by the Ni/C@SiO$_2$-800. Reaction conditions: 50 mmol nitrobenzene, 5 mg catalyst, 20 mL ethanol, 2 MPa H$_2$, 50 °C.

intermediate and then hydrogenated to *N*-hydroxyaniline very quickly, and the hydrogenation of hydroxylamine to aniline was the rate-determining step.[48] For the NiCu/C@SiO$_2$-800 catalyst, the selectivity of the intermediate *N*-hydroxyaniline was always less than 2.7% for the whole process, and declined to zero when the reaction time was prolonged to 2 h (Fig. 4a). However, when Ni/C@SiO$_2$-800 was used as the catalyst in the hydrogenation of nitrobenzene, a considerable amount of *N*-hydroxyaniline was observed, with a nearly 35% selectivity at low nitrobenzene conversion (Fig. 4b). These results demonstrated that the NiCu/C@SiO$_2$-800 was more favorable for quickly reducing the adsorbed *N*-hydroxyaniline intermediate to aniline in comparison with Ni/C@SiO$_2$-800. Based on the above catalytic activity studies and previous XPS analysis, it was suggested that the electronic interaction between Ni and Cu atoms facilitated the generation of electron-deficient Ni active sites, which favoured the adsorption of electron-enriched substances (that is, *N*-hydroxyaniline) on the Ni surface, accelerated the hydrogenation of *N*-hydroxyaniline into aniline and, in turn, improved the nitrobenzene conversion. Therefore, the excellent catalytic performance of the NiCu/C@SiO$_2$-800 catalyst could be

attributed to the combination of two factors: first, the small metal nanoparticles offered more active sites than the large ones; second, the electronic interaction between Ni and Cu atoms improved the intrinsic activities of Ni active sites.

The hydrogenation of nitrobenzene was further employed to investigate the stability and reusability of the NiCu/C@SiO$_2$-800 and Ni/C@SiO$_2$-800 catalysts for comparison. As presented in Fig. 5, under the studied conditions, the NiCu/C@SiO$_2$-800 catalyst exhibited a nitrobenzene conversion of 91.1% in the first cycle, and can be reused at least 10 times with a nitrobenzene conversion still about 80.8% after the 10th run. However, for the Ni/C@SiO$_2$-800 catalyst, a remarkable decrease in the nitrobenzene conversion took place in the 2nd cycle, and it became almost completely deactivated after 4 uses. The spent catalysts were further characterized by XRD, TEM, and XPS. The XRD and TEM results revealed that the phase structure and metal particle size of the spent NiCu/C@SiO$_2$-800 and Ni/C@SiO$_2$-800 catalysts did not change after 10 cycles (Fig. S2 and S3, ESI†). As shown in Fig. 6, the relative peak areas of Ni^{2+} on the NiCu/C@SiO$_2$-800 catalyst surfaces were slightly increased as compared with the freshly prepared catalysts. However, as for the Ni 2p XPS spectra of spent Ni/C@SiO$_2$-800, all of the metallic Ni species were oxidized after recycling. These results demonstrated that the alloying of Ni and Cu atoms may be helpful for protecting Ni species from being oxidized into NiO, which contributed to the excellent anti-oxidation ability and superior recyclability of the NiCu/C@SiO$_2$-800 catalyst.

For the verification of the general applicability of the NiCu/C@SiO$_2$-800 catalyst, the hydrogenation of other nitro compounds was also investigated, and the results are listed in Table 2. The effect of the electronic properties of the substituted groups on the catalytic activity was significant, in general, nitroarenes bearing electron-donating substituent groups, such as –CH$_3$, –OH, –NH$_2$, and –OCH$_3$ (entries 2–8) showed higher
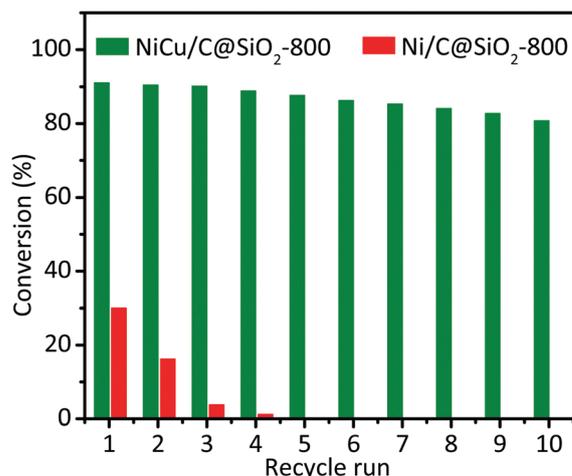

Fig. 5   Reusability profiles of the NiCu/C@SiO$_2$-800 and Ni/C@SiO$_2$-800 catalysts for the hydrogenation of nitrobenzene to aniline with H$_2$. Reaction conditions: 200 mmol nitrobenzene, 20 mg catalyst, 80 mL ethanol, 2 MPa H$_2$, 120 °C, 0.5 h.
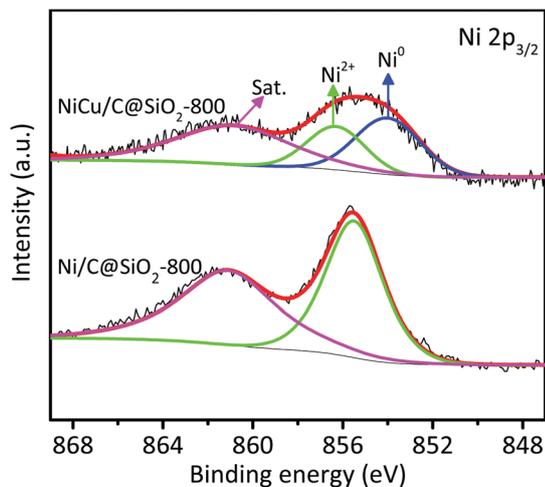
Fig. 6 Ni 2p XPS spectra of the spent NiCu/C@SiO$_2$-800 and Ni/C@SiO$_2$-800 samples.

Table 2 Catalytic hydrogenation of nitroarenes into amines by H$_2$ catalyzed by NiCu/C@SiO$_2$-800[a]

nitrile, and sulfanilamide substituted nitroarenes could be selectively transformed to the corresponding aromatic amines without reduction of these reducible functional groups (entries 12–18). Moreover, a high catalytic performance was obtained in the hydrogenation of heterocyclic nitroarenes containing N element (entries 18 and 19) without detectable byproducts. These results demonstrated that the bimetallic NiCu/C@SiO$_2$-800 catalyst displayed excellent catalytic activity and high selectivity for the hydrogenation of various functionalized nitro aromatics using H$_2$ as the reducing agent.

4 Conclusions

In summary, highly stable non-noble NiCu/C@SiO$_2$ catalysts have been prepared by one-step impregnation and *in situ* carbothermal reduction methods. Compared with the monometallic Ni/C@SiO$_2$-800 catalyst, the addition of Cu not only dramatically improves the catalytic activity (TOF = 46.5 s^{-1}) of the NiCu/C@SiO$_2$-800 catalyst for the hydrogenation of nitrobenzene to aniline, but also enhances the anti-oxidation ability of the catalyst. The remarkable catalytic activity of the NiCu/C@SiO$_2$ derives from the small Ni particles and the electronic interaction between Ni and Cu atoms. The NiCu/C@SiO$_2$-800 catalyst can be reused for the hydrogenation of nitrobenzene without a decrease in catalytic efficiency, and highly efficiently and quantitatively transforms various substituted nitro aromatics to the corresponding aromatic amines with high selectivities. The present study can be extended to design other low-cost and high-performance non-noble metal-based bimetallic catalysts for various catalytic reactions.

Author contributions

Yao Sheng conceived the idea, offered guidance to Xinrui Lin on experiments, and edited the manuscript. Xinrui Lin performed laboratory experiments and characterization. Shengnan Yue carried out TEM. Yang Liu and Xiujing Zou conducted part of the characterization analysis of the material. Xueguang Wang and Xionggang Lu were responsible for planning and supervising the project.

Conflicts of interest

There are no conflicts of interest to declare.

Acknowledgements

Notes and references

1 M. Tian, X. Cui, M. Yuan, J. Yang, J. Ma and Z. Dong, *Green Chem.*, 2017, **19**, 1548–1554.
2 T. M. Bustamante, C. H. Campos, M. A. Fraga, J. L. G. Fierro and G. Pecchi, *J. Catal.*, 2020, **385**, 224–237.

[a] Reaction conditions: 50 mmol nitroarenes, 5 mg catalyst, 20 mL ethanol, 2 MPa H$_2$, 120 °C. [b] Conversions were detected by GC. [c] Selectivity at 100% conversion of nitroarenes. The TOFs were calculated from the initial substrate conversions of less than 20%.

reactivity compared to the substrates with electron-withdrawing groups (entries 9–16). Notably, it was found that carboxyl, ester,

3 G. Zhang, F. Tang, X. Wang, P. An, L. Wang and Y.-N. Liu, *ACS Sustainable Chem. Eng.*, 2020, **8**, 6118–6126.

4 H. Pang, F. Gallou, H. Sohn, J. Camacho-Bunquin, M. Delferro and B. H. Lipshutz, *Green Chem.*, 2018, **20**, 130–135.

5 Y. Sheng, X. Wang, Z. Xing, X. Chen, X. Zou and X. Lu, *ACS Sustainable Chem. Eng.*, 2019, **7**, 8908–8916.

6 C. Chen, R. Fan, M. Han, X. Zhu, Y. Zhang, H. Zhang, H. Zhao and G. Wang, *Appl. Catal., B*, 2021, **280**, 119448.

7 Y. Wang, R. Qin, Y. Wang, J. Ren, W. Zhou, L. Li, J. Ming, W. Zhang, G. Fu and N. Zheng, *Angew. Chem., Int. Ed.*, 2020, **59**, 12736–12740.

8 L. Lin, S. Yao, R. Gao, X. Liang, Q. Yu, Y. Deng, J. Liu, M. Peng, Z. Jiang, S. Li, Y.-W. Li, X.-D. Wen, W. Zhou and D. Ma, *Nat. Nanotechnol.*, 2019, **14**, 354–361.

9 A. Goswami, R. G. Kadam, J. Tuček, Z. Sofer, D. Bouša, R. S. Varma, M. B. Gawande and R. Zbořil, *Chem. Eng. J.*, 2020, **382**, 122469.

10 X. Chen, S. Song, H. Li, G. Gözaydın and N. Yan, *Acc. Chem. Res.*, 2021, **54**, 1711–1722.

11 Y. Wang, S. Furukawa, X. Fu and N. Yan, *ACS Catal.*, 2019, **10**, 311–335.

12 H. Huang, X. Wang, X. Li, C. Chen, X. Zou, W. Ding and X. Lu, *Green Chem.*, 2017, **19**, 809–815.

13 W. She, T. Qi, M. Cui, P. Yan, S. W. Ng, W. Li and G. Li, *ACS Appl. Mater. Interfaces*, 2018, **10**, 14698–14707.

14 Y. Ren, H. Wei, G. Yin, L. Zhang, A. Wang and T. Zhang, *Chem. Commun.*, 2017, **53**, 1969–1972.

15 H. Wang, X. Li, X. Lan and T. Wang, *ACS Catal.*, 2018, **8**, 2121–2128.

16 F. Yang, M. Wang, W. Liu, B. Yang, Y. Wang, J. Luo, Y. Tang, L. Hou, Y. Li, Z. Li, B. Zhang, W. Yang and Y. Li, *Green Chem.*, 2019, **21**, 704–711.

17 W. Kang, H. Guo and A. Varma, *Appl. Catal., B*, 2019, **249**, 54–62.

18 Y. Wang, S. Furukawa and N. Yan, *ACS Catal.*, 2019, **9**, 6681–6691.

19 C. Cui, Y. Liu, S. Mehdi, H. Wen, B. Zhou, J. Li and B. Li, *Appl. Catal., B*, 2020, **265**, 118612.

20 L. Zeng, Y. Wang, Z. Li, Y. Song, J. Zhang, J. Wang, X. He, C. Wang and W. Lin, *ACS Appl. Mater. Interfaces*, 2020, **12**, 17436–17442.

21 N. Zhang, Y. Yi, J. Lian and Z. Fang, *Chem. Eng. J.*, 2020, **395**, 124897.

22 J. Li, M. Li, C. Zhang, C.-L. Liu, R.-Z. Yang and W.-S. Dong, *J. Catal.*, 2020, **381**, 163–174.

23 Y.-R. Zhang, B.-X. Wang, L. Qin, Q. Li and Y.-M. Fan, *Green Chem.*, 2019, **21**, 1108–1113.

24 A. Y. Faid, A. O. Barnett, F. Seland and S. Sunde, *Electrochim. Acta*, 2021, **371**, 137837.

25 M. A. Ahsan, A. R. Puente Santiago, Y. Hong, N. Zhang, M. Cano, E. Rodriguez-Castellon, L. Echegoyen, S. T. Sreenivasan and J. C. Noveron, *J. Am. Chem. Soc.*, 2020, **142**, 14688–14701.

26 R. Li, W. Yao, Y. Jin, W. Jia, X. Chen, J. Chen, J. Zheng, Y. Hua, D. Han and J. Zhao, *Chem. Eng. J.*, 2018, **351**, 995–1005.

27 H. Liu, Z. Huang, H. Kang, X. Li, C. Xia, J. Chen and H. Liu, *Appl. Catal., B*, 2018, **220**, 251–263.

28 T. Q. N. Tran, B. J. Park, W. H. Yun, T. N. Duong and H. H. Yoon, *Sci. Rep.*, 2020, **10**, 1–10.

29 Z. Chen, R. Wu, Y. Liu, Y. Ha, Y. Guo, D. Sun, M. Liu and F. Fang, *Adv. Mater.*, 2018, **30**, 1802011.

30 J. Peng, N. Chen, R. He, Z. Wang, S. Dai and X. Jin, *Angew. Chem., Int. Ed.*, 2017, **129**, 1777–1781.

31 J. Zhao, L. Yang, F. Li, R. Yu and C. Jin, *Carbon*, 2009, **47**, 744–751.

32 D. Li, M. Lu, K. Aragaki, M. Koike, Y. Nakagawa and K. Tomishige, *Appl. Catal., B*, 2016, **192**, 171–181.

33 Y. Liu, J. Zhao, J. Feng, Y. He, Y. Du and D. Li, *J. Catal.*, 2018, **359**, 251–260.

34 J. Wu, G. Gao, J. Li, P. Sun, X. Long and F. Li, *Appl. Catal., B*, 2017, **203**, 227–236.

35 C. Gu, D. Wu, M. Wen and Q. Wu, *Dalton Trans.*, 2018, **47**, 7083–7089.

36 Y. Zhang, C. Liu, G. Fan, L. Yang and F. Li, *Dalton Trans.*, 2018, **47**, 13668–13679.

37 Y. Zhai, C. Li, G. Xu, Y. Ma, X. Liu and Y. Zhang, *Green Chem.*, 2017, **19**, 1895–1903.

38 W. Li, Y. Zhao, Y. Liu, M. Sun, G. I. N. Waterhouse, B. Huang, K. Zhang, T. Zhang and S. Lu, *Angew. Chem., Int. Ed.*, 2021, **60**, 3290–3298.

39 M. F. Sanad, A. R. Puente Santiago, S. A. Tolba, M. A. Ahsan, O. Fernandez-Delgado, M. S. Adly, E. M. Hashem, M. M. Abodouh, M. S. El-Shall, S. T. Sreenivasan, N. K. Allam and L. Echegoyen, *J. Am. Chem. Soc.*, 2021, **143**, 4064–4073.

40 H. Yen, Y. Seo, S. Kaliaguine and F. Kleitz, *ACS Catal.*, 2015, **5**, 5505–5511.

41 P. Yin, X. Luo, Y. Ma, S.-Q. Chu, S. Chen, X. Zheng, J. Lu, X.-J. Wu and H.-W. Liang, *Nat. Commun.*, 2021, **12**, 3135.

42 J. Cai, Y. Zhuang, Y. Chen, L. Xiao, Y. Zhao, X. Jiang, L. Hou and Z. Li, *ChemCatChem*, 2020, **12**, 6241–6247.

43 C. Cheng, P. Li, W. Yu, D. Shen, X. Jiang and S. Gu, *ACS Sustainable Chem. Eng.*, 2020, **8**, 16217–16228.

44 Y. Zhao, S. Li, Y. Wang, B. Shan, J. Zhang, S. Wang and X. Ma, *Chem. Eng. J.*, 2017, **313**, 759–768.

45 C. Liao, B. Liu, Q. Chi and Z. Zhang, *ACS Appl. Mater. Interfaces*, 2018, **10**, 44421–44429.

46 P. Zhou, L. Jiang, F. Wang, K. Deng, K. Lv and Z. Zhang, *Sci. Adv.*, 2017, **3**, e1601945.

47 R. Millán, L. Liu, M. Boronat and A. Corma, *J. Catal.*, 2018, **364**, 19–30.

48 J. Song, Z.-F. Huang, L. Pan, K. Li, X. Zhang, L. Wang and J.-J. Zou, *Appl. Catal., B*, 2018, **227**, 386–408.